Synthesis of Superconducting Nanocables of FeSe Encapsulated in Carbonaceous Shell

Sukhada Mishra,[†] Kai Song,[‡,∥] Jakub A. Koza,[†] and Manashi Nath[†,*]

[†]Department of Chemistry and [‡]Materials Research Center, Missouri University of Science and Technology, Rolla, Missouri 65409, United States.
[∥]Present address: FEI Company, 5350 NE Dawson Creek Drive, Hillsboro, Oregon 97124, United States.

ABSTRACT The recent discovery of superconductivity in iron selenide has attracted considerable attention due to the simplicity of composition, unconventional nature of superconductivity, and ease of synthesis. We have synthesized superconducting FeSe nanowires with a simple catalyst-aided vapor transport reaction at 800 °C in an inert atmosphere. The precursors were chosen to be elemental Se and iron acetylacetonate [$Fe^{III}(C_5H_8O_2)_3$]. These vaporized very easily, thereby facilitating transport, and also contributed to the formation of a carbonaceous shell encapsulating the FeSe nanowires. The superconductivity of these nanocables was confirmed through magnetic measurements and a T_c of ≈8 K was obtained for an ensemble of nanocables. The length of FeSe filling inside the carbon nanofibers could be varied by controlling the reaction conditions while the diameter of nanowires was dependent on the thickness of Au–Pd coating used as a catalyst. Extensive analysis through high-resolution microscopy revealed that there was considerable lattice contraction of FeSe in the nanocable up to about 3.6% along the *c*-direction leading to a reduced spacing between the (001) lattice planes. Interestingly, this compression was more pronounced near the catalyst-FeSe interface and was reduced further along the length of the nanocable. The presence of carbon nanofibers as a shell around the FeSe protected the FeSe nanowires from both atmospheric O_2 and moisture attack, as was evident from the very long ambient condition shelf life of these nanocables, and also makes them more stable under e-beam irradiation.

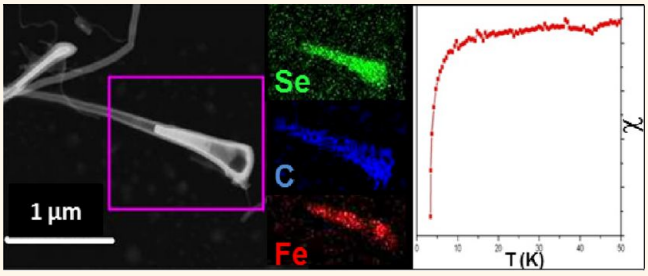

KEYWORDS: FeSe nanowires · superconducting nanowires · pnictide superconductors · core–shell nanowires

The discovery of superconductivity in LaFePO in 2006 by Hosono and coworkers[1] marked the onset of a new family of iron-based superconductors. It also began an era of unconventional superconductors, which has been termed "*the iron age of superconductivity*". These new superconductors belong to the iron pnictide families, generally referred to as [1111] (*Ln*Fe*Pn*O, *Ln* = lanthanides, *Pn* = P, As);[2−4] [122] (A′A″Fe_2As_2 A′ = K; A″ = Ba, Sr, Eu);[5,6] [111] (*A*FeAs, *A* = Li, Na);[7,8] and the chalcogenide FeSe (011).[9] Current progress in this field has been compiled in several extensive reviews.[10−14] The presence of superconductivity in an Fe-based compound itself is fascinating because Fe is more popularly known for having magnetic ordering, which does not preferably coexist with superconductivity. The common motif present in Fe-based superconductors is a Fe_2Pn_2 layer (*Pn* = As, P), where Fe is tetrahedrally coordinated to *Pn* in the anionic layer and the cationic layers play a significant role of charge reservoirs. One of the simplest compounds containing similar Fe_2Pn_2 layers, as found in these superconductors, is a PbO-type tetragonal FeSe. In fact, in 2008, FeSe, a simple binary compound, demonstrated superconductivity at 8 K without any chemical doping.[9] FeSe has two major phases, a Se-deficient tetragonal phase where superconductivity was initially observed[9] and an Fe-deficient phase that is a stoichiometric variant of the NiAs structure type.[15] The structure of superconducting FeSe is built by edge sharing of the $FeSe_4$ tetrahedra where both Fe and Se are 4-coordinated.[16] Analogous to other iron-based superconductors, FeSe also exhibits an enhancement in T_c through chemical doping with Te in the anionic site (T_c = 21 K).[17] More interestingly, the T_c in this tetragonal FeSe is pressure-sensitive and can be increased significantly (36.5 K) by applying external pressure.[18,19]

* Address correspondence to nathm@mst.edu.

Received for review September 12, 2012 and accepted January 30, 2013.

Published online January 30, 2013
10.1021/nn3056669

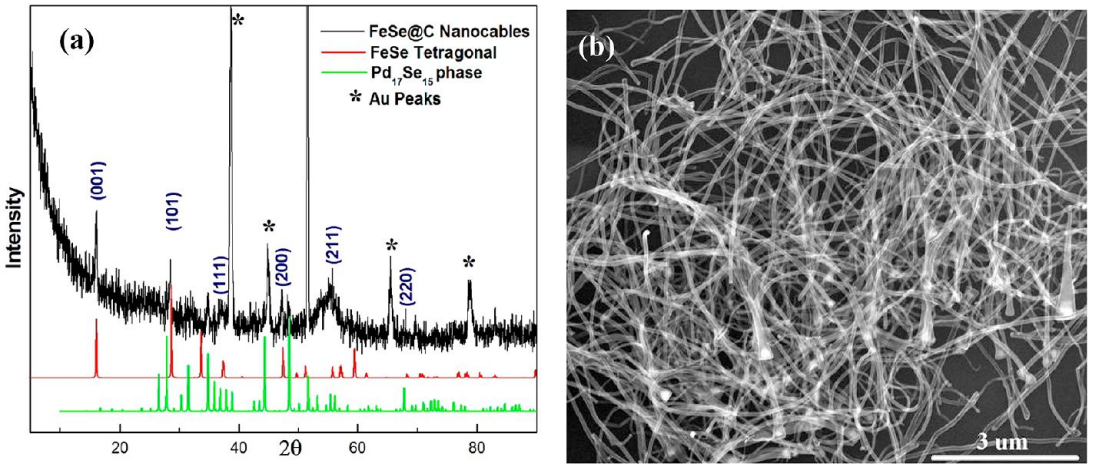

Figure 1. (a) PXRD pattern of the nanowires showing a mixture of tetragonal FeSe and cubic $Pd_{17}Se_{15}$ along with Au peaks. (b) SEM image showing huge yield of nanowires over the Si substrate.

Superconductivity in low-dimensional materials is of huge interest to researchers working in this field. It has been reported that superconductivity can be suppressed in ultrathin nanowires of simple elemental and alloy superconductors due to thermal and quantum phase slips.[20,21] The critical current on the other hand increases significantly with decreasing diameter of superconducting nanowires.[22,23] Theoretical studies on finite size effects in pnictide superconductors have led to the belief that both critical current and T_c can be affected in low-dimensional structures.[24] This finding is especially important for the Fe-based superconductors that inherently exhibit both high critical fields and critical current density.[10,11,14] Superconducting nanowires are also important technologically, as ideally they can provide a dissipationless flow of current in complex nanodevices. They can also facilitate high-efficiency power transmission and offer potential applications in photodetectors,[25] superconducting gravimeters,[26] single-photon detectors,[27,28] and quantum electronics.[29] Iron-based superconductors, by virtue of their unconventional nature, are expected to demonstrate a change in not only their magnetic but also their electronic properties on nanostructuring, thereby affecting their superconducting properties.[30] To date, several superconducting nanowires, including those of simple metals,[31] cuprates [YBCO],[32] and recently, MgB_2[33,34] have been synthesized through various techniques, including vapor transport, sol−gel synthesis, electrodeposition, and lithographic pattern transfer.[20−22,32−34] However, there are very few reports on the synthesis of FeSe nanostructures to date.[35,36] Traditional techniques for synthesizing FeSe such as pulsed laser deposition,[37] the selenization of Fe films,[38] and solid state reactions[39] require drastic conditions, thereby leading to bulk morphology. FeSe nanorods were recently synthesized using chemical vapor deposition methods,[40] with H_2Se as the selenium source. In this paper we present a simple synthesis method for growing FeSe nanowires through one-step, catalyst-aided vapor transport reaction.

RESULTS AND DISCUSSIONS

Synthesis of FeSe@C Nanocables. FeSe nanowires were synthesized by chemical vapor deposition, under N_2 flow at 800 °C in a horizontal tube furnace equipped with a mass flow controller. In this approach for the synthesis of FeSe nanowires, the key feature was the choice of the precursors, iron acetylacetonate [$Fe(acac)_3$] and Se, both subliming very easily at 180 and 400 °C, respectively. These sublimable precursors were expected to assist in the formation of nanowires. A catalyst-coated Si wafer, maintained at 800 °C, was used as a substrate to grow the nanostructures, while $Fe(acac)_3$ and Se were kept at the desired temperatures to maintain a steady flow of the precursors. Further details of the experimental setup are provided in the Methods section. After the completion of the reaction, the Si substrate was covered with a blackish product. This was further characterized thoroughly through powder X-ray diffraction (pxrd), scanning and tunneling electron microscopy (SEM, TEM respectively), scanning tunneling electron microscopy (STEM), high angle annular dark field imaging (HAADF), magnetic characterization, X-ray photoelectron spectroscopy (XPS), energy dispersive spectrometry (EDS), and Raman analysis to get an insight into the product morphology, phase, and elemental composition.

Structural and Morphology Characterization. Figure 1a shows the pxrd pattern of the product, confirming the presence of tetragonal FeSe (JCPDS card number 04-001-9129) along with the peaks for Au used as catalyst. Interestingly, the cubic phase of $Pd_{17}Se_{15}$ (JCPDS card number 00-011-0508) was also observed as shown in the Figure 1a. Peaks of tetragonal FeSe could be indexed according to the standard pattern (JCPDS card number 04-001-9129). It should be noted here that few FeSe peaks were indiscernible in the

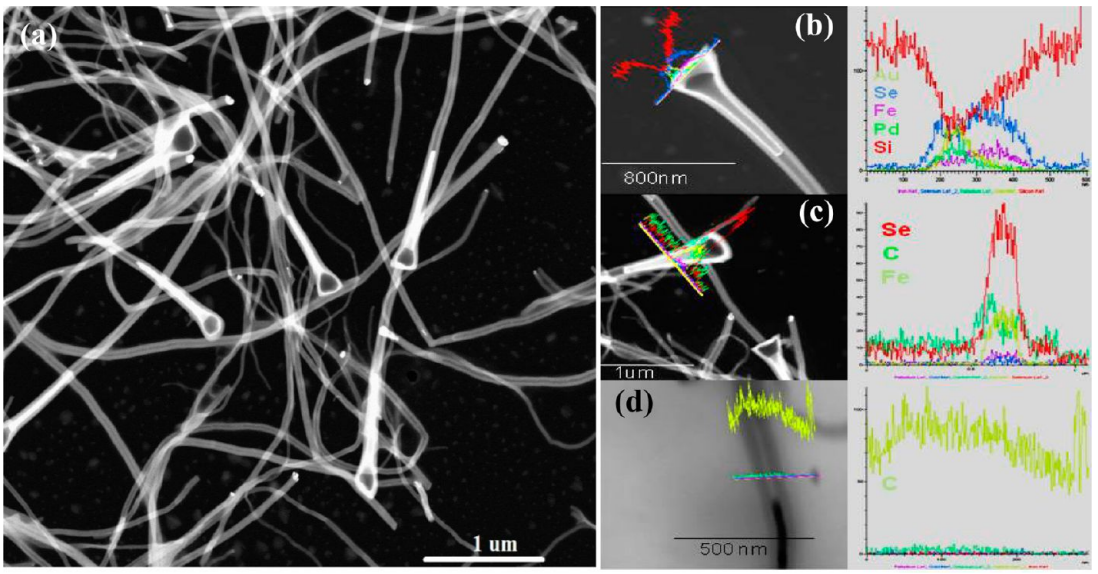

Figure 2. (a) Low magnification STEM image of the formed nanocables, showing core−shell type of morphology along with nanocable tip. (b−d) Elemental analysis through line scan at the (b) tip of the nanocable showing the presence of Au, Pd, C, Se, and Fe (right panel), (c) in the filling part showing Fe, Se, and C predominantly and minimal Au and Pd, and (d) in the tube, confirming the presence of carbon nanofibers.

experimental pxrd pattern, probably due to orientation effect and anisotropy in the formed nanostructures. The pxrd pattern demonstrated a broad feature at the 2θ range of 52−57°, which can be attributed to the presence of several closely spaced peaks for $Pd_{17}Se_{15}$ that also overlaps with the peaks for tetragonal FeSe, effectively giving rise to a broad peak. It was observed that the pxrd pattern showed weak intensities and low signal-to-noise ratio of the diffraction peaks. This could be attributed to the fact that the pxrd pattern was collected from powder spread over Si substrate where the high crystallinity of the Si background created obstructive scattering noise from the substrate. Also, the actual amount of FeSe and $Pd_{17}Se_{15}$ in the product was only a fraction of the total mass (*vide infra*), thereby reducing the signal intensity even more. The thickness of the FeSe nanostructure as estimated from the Debye−Scherrer equation[41] was ∼23 nm.

SEM, as shown in Figure 1b, exhibited a high yield of nanowires, with lengths exceeding several micrometers and diameters in the range of 30−70 nm. Careful observation of the STEM images, however, revealed that the nanostructures possess a peculiar, core−shell type of morphology, as shown in Figure 2a. These nanostructures consisted of hollow tubules filled with solid material where the tip of the filling is typically darker in contrast, giving them the appearance of a "*nanocable*". The diameter of the filling was 20−50 nm and the length of the individual tubules varied from 5 to 10 μm. EDS analysis demonstrated the presence of elemental Fe and Se in a 1:1 ratio in these one-dimensional nanostructures, confirming the formation of FeSe (Supporting Information, Figure S1). A detailed elemental analysis of the nanocables was performed through EDS line scans collected from different locations along the nanocable length to determine the composition of the nanocable tip, filling, and tube wall. Figure 2b illustrates the line scan performed at the tip of the nanocable, revealing the presence of both Au and Pd catalyst as major components along with trace amounts of Fe and Se. Figure 2c illustrates the line scan collected from the body of the filling. In this region, both Fe and Se appeared to be the major components along with C and negligible amounts of Au and Pd. Interestingly, the C signal (green line) peaked near the tube walls, indicating there was less C in the filling itself. Figure 2d illustrates the line scan performed across the tubule where there was no filling, clearly showing that the C signal was most intensified with a negligible amount of Se, Fe, Au, and Pd. Thus, it was concluded that the hollow tubules were comprised of C, while the filling was purely FeSe. Further quantitative and qualitative analysis was performed using X-ray photoelectron spectroscopy (XPS) technique to confirm the chemical composition (Supporting Information, Figure S2a). The XPS spectra collected on the nanocables indicated the presence of elemental Se and C, along with a trace amount of Fe. After sputtering for 20 min which removed approximately 20 nm surface layers of nanocables, the Fe signal increased significantly and the C signal decreased. This type of superconducting nanowire, encapsulated by carbon nanotubes (CNT), has been previously reported for Sn nanowires.[42] Raman spectroscopy was conducted on an ensemble of these nanocables to get a better insight of the carbonaceous shell in these nanocables. Raman analysis demonstrated both a D band and a G band at 1319.30 and

1585.85 cm^{-1}, respectively (Supporting Information, Figure S2b). The area integral intensity ratio of the *D* and *G* peaks (I_D/I_G) in the Raman spectra was calculated to be 3.327, indicating the presence of amorphous carbon in the form of nanofibers.[43] The length of the FeSe filling inside the nanocables could be increased by varying the reaction conditions, including an increase in the concentration of the reactants (Se and $Fe(acac)_3$), whereby, we could successfully extend FeSe filling further away from the tip (Supporting Information, Figure S3). The diameter of the FeSe filling could be somewhat controlled by the diameter of the Au–Pd catalyst particle, where the optimal catalyst thickness was observed to be 50–100 nm. These nanocables were also analyzed through high resolution transmission electron microscopy (HRTEM), which demonstrated crystalline nature of the FeSe filling and offered some valuable insights for understanding the growth mechanism of these FeSe@C nanocables (*vide infra*).

Superconductivity in these nanocables was characterized by DC magnetic susceptibility, measured on an ensemble of nanocables, spread on the Si substrate. Magnetization was measured as a function of temperature, under zero field cooled conditions using, a vibrating sample magnetometer. Figure 3 illustrates a plot of magnetic susceptibility (χ) as a function of temperature, measured with an applied field of 100 Oe. Superconducting transition was clearly observed at ≈8 K, which was in good agreement with the T_c of bulk FeSe.[9] Because the exact mass of the nanocables dispersed over Si could not be precisely determined, the magnetization data could not be normalized with respect to mass. Hence, the magnetization of a blank Si substrate was also measured under similar conditions and used as a reference. As expected the Si substrate by itself did not demonstrate any appreciable transition (Supporting Information, Figure S4). However, the magnetization data from the ensemble was heavily masked by the huge diamagnetic background from both the Si substrate and the carbonaceous shell. Interestingly, the carbonaceous shell did not affect the superconducting T_c of FeSe in these nanocables. This observation is similar to that made by Jankovic *et al.* for their CNT-coated Sn nanowires.[42]

High Resolution TEM Characterization of FeSe@C Nanocables. HRTEM was performed at various regions of the FeSe@C nanocables, as shown in Figure 4a–f. HRTEM revealed lattice fringes of both the FeSe filling and Au–Pd-rich catalyst, which demonstrated a high degree of crystallinity of these phases. The carbon tubule walls, however, did not demonstrate a high degree of crystallinity. Figure 4a illustrates the bright field TEM image of a filled nanocable, which includes regions of different contrast. An EDS line scan along the same nanocable (Figure 4b) indicates that, beginning at the tip, the nanocable has a sequence of Au-rich,

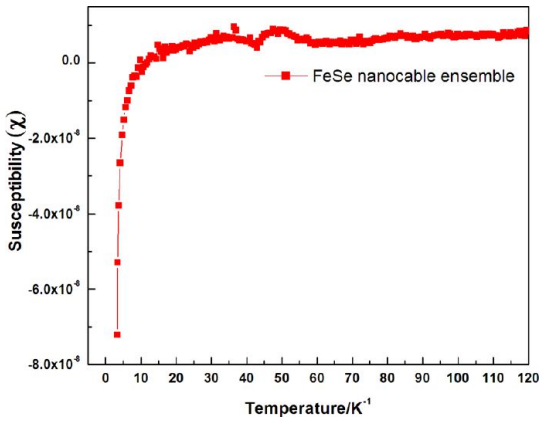

Figure 3. Plot of magnetic susceptibility vs temperature of the FeSe@C nanocables showing the onset of superconductivity at ≈8 K.

Pd–Se-rich, Fe–Se-rich, Pd–Se-rich, and Fe–Se-rich segments, as shown by arrows in the Figure 4a. EDS point analysis collected from the above marked regions also corroborated the proposed element distribution (Supporting Information, Figure S5). The electron diffraction pattern (inset in Figure 4a) obtained from the Au-rich tip confirmed the presence of single crystalline Au. It was observed that, while Au was immobilized at the tip of the nanocable, the Pd part of the bimetallic catalyst actually attached to the growing FeSe (as shown in Figure 4a) and was frequently dislodged from the tip, whereby the Pd-rich segment was located within the FeSe filling (4th arrow from the left in Figure 4a). Figure 4c is a magnified HRTEM image illustrating the interface between the Pd–Se region (on the left) and the Fe–Se region (on the right). The lattice spacing in the Fe–Se region was measured to be 5.32 Å, which is in close agreement with the (001) plane of the tetragonal FeSe phase. The Pd–Se rich region was characterized by electron diffraction (ED) generated by Fast Fourier Transform (FFT) from the lattice fringes (inset of Figure 4c), which indicated the presence of cubic $Pd_{17}Se_{15}$ single crystal. While the majority of the FeSe nanocables showed lattice fringes corresponding to (001) planes, some nanocables, as shown in Figure 4d, exhibited lattice fringes at 3.05 Å corresponding to the (101) plane. HRTEM images shown in Figure 4d were collected from the FeSe filling which was far away from the catalyst tip. The inset in Figure 4d illustrates the experimental electron diffraction pattern from this FeSe filling phase, which contained diffraction spots corresponding to the $(11\bar{3}$ and $1\bar{1}1)$ planes, respectively. Frequently the other end of these nanocables also contained a catalyst tip, as shown in Figure 4e, which shows regions of a different contrast. A magnified, high resolution image of this catalyst tip collected from the region marked by the white box is given in Figure 4f. The lattice spacing from the FeSe region was measured to be 2.61 Å, matching that of the (110) planes of the tetragonal

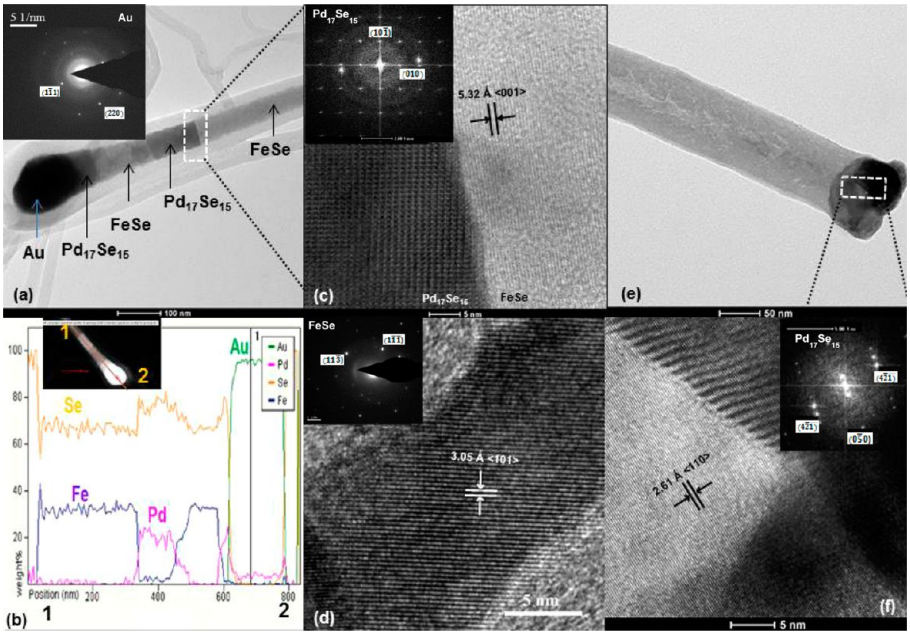

Figure 4. (a) TEM image of the FeSe@C nanocable showing the segregation of Au, $Pd_{17}Se_{15}$, and FeSe along the nanocable length. Inset shows the SAED pattern obtained from the Au region. (b) EDS line scan performed across the length of the nanocable (from position 1−2) tracing the presence of Au, Pd, Fe, and Se at different regions. (c) HRTEM image showing the interface between $Pd_{17}Se_{15}$ and FeSe. Inset shows the FFT pattern generated from the $Pd_{17}Se_{15}$ region. (d) HRTEM image of the FeSe displaced away from the catalyst tip. Inset shows the SAED with the spots indexed to tetragonal FeSe. (e) TEM image of the catalyst tip at the end of the FeSe@C nanocables showing coexistence of $Pd_{17}Se_{15}$ and FeSe. (f) HRTEM image of the catalyst tip showing the interface between FeSe (left side) and $Pd_{17}Se_{15}$ (right side). Inset shows the FFT pattern of the $Pd_{17}Se_{15}$ phase.

FeSe phase. The inset in Figure 4f shows the FFT image of the Pd/Se region, which contained spots corresponding to 2.48, 2.29, and 2.09 Å, matching with the $(4\bar{1}\bar{1})$, $(4\bar{2}1)$ and $(0\bar{5}0)$ planes of the cubic $Pd_{17}Se_{15}$ phase, respectively. Single crystal Si was used as a calibration standard for accurately estimating the lattice spacing from HRTEM images. All calculations for lattice spacing were done by counting at least 30 lattice planes. From these detailed microscopic studies involving HRTEM, EDS line scans, and elemental mapping, it was evident that the nanocables were not pure FeSe, but rather consisted of segments of Au, $Pd_{17}Se_{15}$, and FeSe, thereby forming a composite nanocable. But, it should be noted here that the FeSe segment in the nanocable was chemically pure because there was no evidence of chemical doping with either Pd or Au in the FeSe regions.

Evidence for Lattice Compression of FeSe and Its Effect on T_c. It should be noted that the (001) lattice spacing for the tetragonal FeSe is reported to be 5.52 Å.[15] For the FeSe nanocables, the (001) lattice spacing consistently demonstrated a contraction of ~3.62%. Lattice compression for the FeSe was also observed through a reduction of lattice spacing for other planes such as the (101) plane [3.05 Å (experimental) vs 3.15 Å (reported)], which showed a contraction of ~3.1%, as seen in Figure 4d. Analogous to both (001) and (101) planes of FeSe, the (110) plane of FeSe also indicated a contraction in the lattice spacing. The value obtained from the standard diffraction data was 2.69 Å. This value corresponds with a ~2.97% of lattice contraction along [110]. From the extensive HRTEM and SAED analysis it was evident that the FeSe in these nanocables showed appreciable lattice compression which was maximum along the [001] direction but also noticeable along the [101] and [110] directions. The lattice compression along the *c*-axis (i.e. [001] direction) is very critical in the FeSe superconductors. Previous work by Cava and co-workers have established that on application of external pressure, the FeSe lattice shrinks along the *c*-direction, thereby leading to denser packing of the Fe_2Se_2 layers. This compression along the *c*-direction is accompanied by an enhancement in T_c.[18,19] The compression along the *c*-direction increases with the applied pressure before the FeSe lattice undergoes a total phase transformation to the hexagonal phase at 38 GPa of pressure.[18,19] Hence, it can be expected that in these FeSe nanocables, compression of the lattice along the [001] direction is reflective of some internal pressure effect. The pressure on the FeSe nanocables might be attributed mainly to the presence of FeSe−$Pd_{17}Se_{15}$ interface and also to the effect of restricted growth within the carbonaceous shell. Because T_c in FeSe superconductors is very sensitive to pressure, it might be expected that the lattice compression will show some effect in the T_c of these nanocables. However, the T_c as obtained from magnetization studies of the FeSe nanocable ensemble was ~8 K, as shown in Figure 3.

Hence, to get a better insight into this compression along the [001] direction in the FeSe nanocables

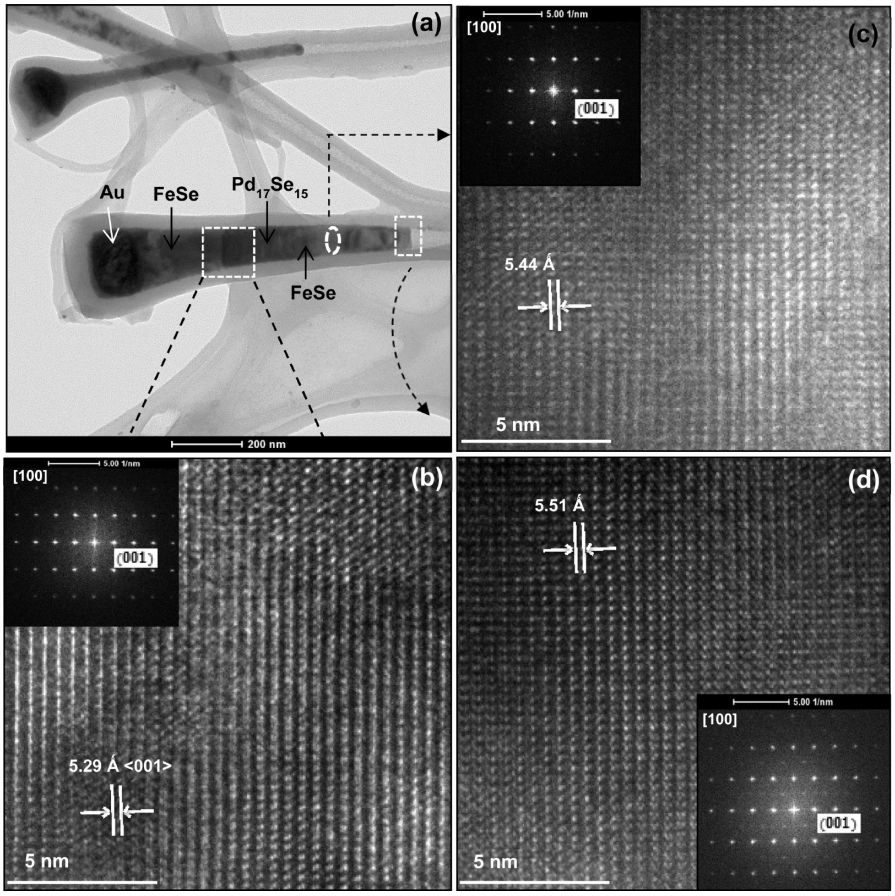

Figure 5. HRTEM images of the FeSe region collected from different sections in the nanocable. (a) Low-magnification image of the nanocable showing different regions (Au, FeSe, $Pd_{17}Se_{15}$), as marked by arrows. (b) FeSe region near the interface [shown by white box in (a)] with lattice fringes corresponding to (001) planes showing a spacing of 5.29 Å. (c) FeSe region at the middle of the nanocable showing a lattice spacing of 5.44 Å for the (001) planes. (d) FeSe region at the end of the nanocable away from the catalyst tip, showing a separation of 5.51 Å between the (001) planes. Inset in (b–d) shows the FFT-generated ED patterns, with diffraction spots corresponding to (001) planes.

extensive HRTEM studies were performed on FeSe region in different parts of the filling (Figure 5a–d), namely, (i) at the interface with the Pd–Se phase; (Figure 5b); (ii) at the middle portion of the FeSe filling (Figure 5c); and (iii) at the open end of the filling (Figure 5d). Figure 5a shows the low magnified image of the nanocables showing different regions, Au, FeSe, and $Pd_{17}Se_{15}$. Figure 5b shows the fringes obtained from the FeSe region close to FeSe/$Pd_{17}Se_{15}$ interface. Inset of Figure 5b indicates FFT obtained from the same region, which could be indexed to (001) planes of tetragonal FeSe. The *d*-spacing corresponding to (001) plane could be calculated (from both the lattice fringes and FFT) as 5.29 Å, which corresponds to approximately 3.8% contraction. Figure 5c shows the fringes obtained from the middle portion of the FeSe filling. It shows the lattice spacing of 5.44 Å, which corresponds to 1.44% lattice contraction. Figure 5d demonstrates HRTEM obtained from the FeSe region corresponding to the open end of the filling. It showed the lattice spacing of 5.51 Å for the (001) planes, which corresponds to 0.1% contraction. These observations indicate that the lattice compression is maximum at the FeSe–$Pd_{17}Se_{15}$ interface and reduces as the FeSe grows away from the interface and is almost negligible at the open end of the FeSe filling. Hence, the amount of FeSe facing this interfacial pressure is only a fraction of the entire nanocable. This might be the reason that the effect on T_c is very minimal. The authors are currently trying to increase the interfacial contact area between the Pd–Se and FeSe phases, thereby expecting a larger lattice compression and enhanced effect on the T_c.

Mechanism of Growth of FeSe@C Nanocables. We varied reaction parameters to gain an insight into the formation mechanism of the FeSe@C nanocable. We soon realized that the role of a bimetallic catalyst is important for formation of the FeSe nanocables. Experiments conducted in the absence of Au–Pd catalysts did not produce any FeSe deposition on the Si substrate. An investigation of the reaction products at lower temperatures (600–800 °C) provided an insight into the mechanism behind the growth of FeSe nanowires. We performed detailed characterization of the intermediate nanostructures through extensive electron microscopy (SEM, TEM, and STEM) and EDS analysis. Figure 6 shows the various stages involved in

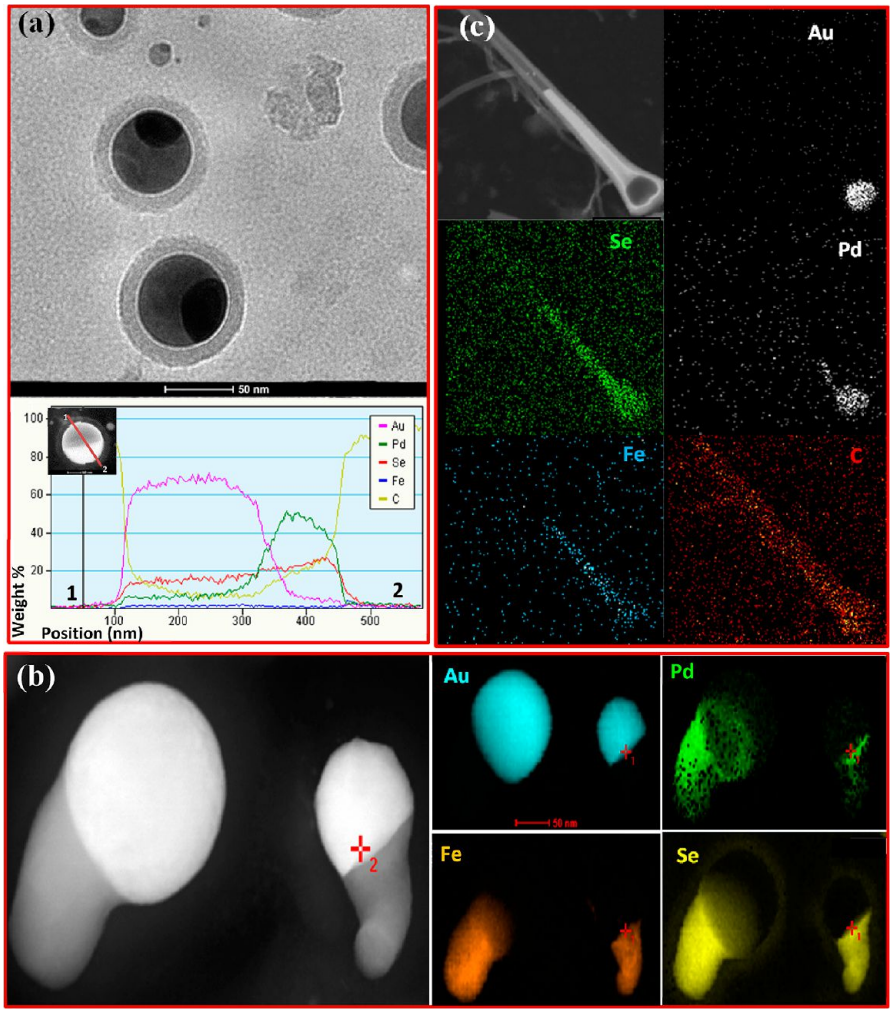

Figure 6. (a) TEM image of the carbon-encapsulated catalyst formed at 600 °C, which shows segregation of Au−Pd. Panel at the bottom shows the EDS line scan performed across the catalyst particle (shown in inset), confirming the presence of Au- and Pd−Se-rich zones, respectively. (b) STEM image of a nanocable in the second stage of growth along with corresponding elemental mappings for Au, Pd, Fe, and Se. The carbonaceous shell was not very visible because it was acquired in the HAADF mode of STEM. (c) Elemental mapping of a fully grown FeSe@C nanocable showing distribution of Au, Pd, Fe, Se, and C along different sections of the nanocable.

the formation of FeSe@C nanocables. During the initial stages of growth, the catalyst particles demonstrated a segregation of Au and Pd, leading to the formation of heterozones, as shown in the TEM image in Figure 6a. The phase segregation of Au and Pd was also confirmed through elemental line scan performed across the bimetallic catalyst (shown in the bottom part of the Figure 6a), which showed two distinct phases: Au in the higher contrast region and Pd−Se in the lower contrast region. It should be noted here that the formation of a carbonaceous shell was very apparent right from the primary stages of nanostructure formation, and the origin of it has been described in detail below. EDS spectra revealed trace amounts of Fe along with Au, Pd, and Se in these biphasic nanoparticles (Supporting Information, Figure S6), demonstrating that, at low temperatures (600 °C), the incorporation of Fe into these nanostructures have just only begun. Fe was present mostly at the Pd-rich edges of the biphasic nanoparticles, indicating that the decomposition and adsorption of Fe precursors were catalyzed by the Pd part of the bimetallic catalyst. In the second stage of growth, Se- and Fe-rich vapors started diffusing in the bimetallic Au−Pd catalyst. Figure 6b shows the elemental mapping from an arrested intermediate stage of growth, where the nanocable has just started growing out from the catalyst end. It demonstrated similar segregation of the Au and Pd regions in the catalyst tip, while the preferential attachment of the growing Fe−Se region to the Pd-end of the catalyst was more visible at this stage. Small migration of $Pd_{17}Se_{15}$ near the growing Pd−FeSe interface was also very apparent in the elemental mapping, which showed that, while Pd is most concentrated near the catalyst tip (upper left-hand region of the Pd map in Figure 6b), there is a minor spreading of Pd into the Fe-rich region. Se mapping indicates the spread of Se over the entire Pd- and Fe-rich regions. As the mapping was

performed in the STEM mode of TEM, the brighter contrast of carbon shell was not visible in the STEM image. As the reaction progressed, a continuous supply of iron from the precursor into the growing nanofibers through surface diffusion formed the thermodynamically stable FeSe filling. As the reaction continues, the formed FeSe further gets filled up inside the carbonaceous shell and led to the formation of nanocables. Figure 6c demonstrates the elemental mapping of the fully grown nanocable. The segregation of the bimetallic catalyst is carried over to the nanocables also, where the Au catalyst remains at the tip away from the FeSe, while the FeSe forms an interface with $Pd_{17}Se_{15}$, which also gets diffused in the growing nanocables near the catalyst−FeSe interface.

The formation of C nanofibers was highly unanticipated in this reaction scheme. The choice of the iron precursor, however actually facilitated the formation of C nanofibers. During the reaction, $Fe(acac)_3$ was not only a source of iron but also a huge reservoir of carbon. These factors gave rise to an ideal condition for the growth of carbon nanofibers encapsulating the formed FeSe. Previous studies indicate that, the multiwall carbon nanotubes forms readily on the Au−Pd catalyst.[44] As the reaction progresses, the carbon species generated through a decomposition of $Fe(acac)_3$ both dissolves and diffuses into the liquid catalyst. At supersaturation of the catalyst, the carbon gets precipitated out as nanofibers.

Binary Phase Diagrams of Au−Pd, Pd−Fe, Pd−Se, and Fe−Se Systems. To understand the different activities of the Au and Pd zone of the bimetallic catalyst toward formation of the FeSe phase, we looked at the binary phase diagrams of Au−Pd, Pd−Fe, Au−Se, and Pd−Se systems.[45−48] From the Au−Pd binary phase diagram it was evident that they mostly exist as solid solution and do not form any stable alloy till about 1100 °C above which they form the molten phases.[45] Hence, the segregation of the bimetallic catalyst into the Au-rich and Pd-rich zones as the reaction temperature was raised to 800 °C could be explained. The Au−Fe phase diagram shows minimal miscibility of these two elements at 800 °C.[46] The Fe−Pd phase diagram on the other hand revealed that, in the Pd excess region, stable alloys like FePd and $FePd_3$ can be formed above 250 °C.[47] This indicates that Fe has a better miscibility with Pd than with Au, and hence, in the present case, as the $Fe(acac)_3$ precursor is transported over the catalyst particle and decomposes, the Pd zone of the catalyst particle will preferentially act as the nucleation point for VLS growth. As Se vapors are transported in the reaction zone, it gets dissolved into the Pd−Fe rich zone of the catalyst, thereby forming the selenides. The Pd−Se binary phase diagram reveals that in the excess Se zone, $Pd_{17}Se_{15}$ is one of the stable intermediates before it goes to $PdSe_2$.[48] The miscibility of Fe with Pd, and the preferential stability of the Pd- and Fe-selenides leads to Pd-end of the catalyst being the active growth zone, while Au is immobilized at the nonparticipating end. Hence, as the nanofiber is being filled up with FeSe, the catalyst-filling (FeSe) interface at the Pd-end will play a very definitive role in defining the crystal structure of the FeSe filling. The authors are trying to investigate this theme further by attempting synthesis of FeSe nanostructures catalyzed by pure Pd nanoparticles, which may show interesting variation in the properties.

CONCLUSION

In conclusion, we have successfully developed a protocol for the synthesis of the superconducting FeSe ($T_c \approx 8$ K) nanocables surrounded by a carbonaceous shell. The simplicity of the process makes it viable for a large-scale production of the superconducting nanocables. The nanocables reported in this paper indicate an ∼3.65% compression of the FeSe lattice along the *c*-direction where the compression is more near the catalyst−FeSe interface and reduces further along the length. The presence of an interface between the Pd-rich phase and FeSe, in combination with restricted growth, may lead to a build-up of internal pressure acting on FeSe, resulting in compression of the lattice. Because the T_c in the FeSe superconductors is extremely pressure-sensitive, this type of nanostructure will be more useful when investigating the effect of morphology on the T_c. For example, we are currently trying to increase the catalyst−FeSe interface while preserving the nanostructured morphology, thereby expecting to see a much more contraction in the *c*-direction of FeSe and significant enhancement in T_c. The distinguishing factor is that the carbonaceous shell does not destroy the superconducting characteristics of the FeSe. It may instead protect the FeSe from undergoing either aerial oxidation or any other atmospheric damage, both of which may lead to either the destruction or inhibition of superconducting properties. These types of superconducting nanocables can be of significant technological importance because the superconductors, being already encapsulated by carbon nanofibers, provide an assembly that can be further utilized for the superconducting FET device manufacturing.

METHODS

Synthesis of FeSe@C Nanocables. Core−shell FeSe@C nanocables were grown on a Si substrate (Si quest international) by chemical vapor deposition. These Si substrates were cut into pieces of 1 × 1 cm^2 and prewashed with isopropanol and acetone in order to remove dirt particles. These substrates were

then sputter-coated with Au−Pd (3:2) for 120 s, creating a thick layer of (approximately 100 nm) Au−Pd over the substrates.

A chemical vapor deposition with a horizontal tube furnace assembly was utilized to synthesize the FeSe@C nanocables. Silicon substrates were kept at the central region of the horizontal furnace at 800 °C. With the help of a mass flow controller the reaction assembly was maintained at a continuous N_2 flow of 180 sccm. Both iron(III) acetylacetonate (99% purity, STREM chemicals) and selenium shots (1−3 mm, amorphous, 99.999%) were chosen to be the precursors for Fe and Se, respectively. Selenium shots were positioned at 400 °C; the $Fe(acac)_3$ was kept at a 180 °C region. Initially, The $Fe(acac)_3$ and Se were kept outside the heating zone by pushing the ceramic liner to the extreme left. Once the central zone of the furnace reached the reaction temperature (800 °C), the ceramic liner was pushed to the right such that the Se and $Fe(acac)_3$ were at 400 and 180 °C, respectively. These steps were crucial for reproducibility of the reaction, as it avoids the sublimation and escape of the reactants (Se and $Fe(acac)_3$vapors) before the Au−Pd catalyst reaches the melting temperature. The reaction was conducted for 30 min, and the furnace was cooled down at the rate of 8 °C/min. After the reaction was completed, we observed a grayish black deposition on the silicon substrate.

Characterization of the Nanocables. *Powder X-ray Diffraction.* The product was characterized without any subsequent purification through powder X-ray diffraction (Philips X-Pert) using Cu Kα (1.5418 Å). Because the product formed a very thin layer on the Si substrate, the pxrd was collected at grazing angles in thin film geometry (GI mode with Göbel mirrors).

Electron Microscopy Characterizations. Scanning electron microscope imaging was performed using FEI Helios NanoLab 600 FIB/FESEM directly onto the Si substrate covered with the nanocables. TEM images were obtained on FEI Tecnai F20 operating at 200 kV. Black powder on Si substrate was both scratched and dispersed in an acetone solution to prepare the TEM sample. A drop of the "as-prepared" solution was placed onto a carbon-coated TEM grid and dried in air prior to TEM imaging and EDS.

Magnetic Characterizations. A magnetic moment was collected from both a SQUID magnetometer and the VSM option of PPMS. The Si substrate containing the FeSe@C nanocables was loaded into a gel cap and was inserted into the magnetometer with the help of standard sample loader. The diamagnetic signal from the gel cap was collected separately and subtracted as a background from the signal obtained from the sample. The ZFC data was obtained after cooling the sample down to ∼2K under 0 magnetic field and then by measuring the magnetic susceptibility warming up data. The susceptibility of a blank Si substrate that was heat treated under conditions (similar to that for FeSe nanocable growth) was also collected and used as a reference.

X-ray Photoelectron Spectrometry. Elemental quantification was performed on a Kratos Axis 165 photoelectron spectrometer. The Si substrate containing an ensemble of the FeSe@C nanocables was analyzed both before and after sputtering. Sputtering was performed for 20 min, which removed an approximately 20 nm layer from the substrate.

Conflict of Interest: The authors declare no competing financial interest.

Supporting Information Available: XPS and Raman analysis, along with EDS elemental quantification data, and the magnetization behavior of Si substrate. This material is available free of charge *via* the Internet at http://pubs.acs.org.

Acknowledgment. The authors would like to acknowledge the Materials Research Center at Missouri University of Science and Technology for allowing us to use their equipment. The authors would also like to thank Dr. Switzer, Seng Huat Lee, and Dr. Hor for their help with magnetic characterizations and Dr. Brow for help with Raman spectroscopy.

REFERENCES AND NOTES

1. Kamihara, Y.; Hiramatsu, H.; Kawamura, R.; Yanagi, H.; Kamiya, T.; Hosono, H. Iron-Based Layered Superconductor: LaOFeP. *J. Am. Chem. Soc.* **2006**, *128*, 10012–10013.
2. Kamihara, Y.; Watanabe, T.; Hirano, M.; Hosono, H. Iron-Based Layered Superconductor $La[O_{1-x}F_x]FeAs$ ($x = 0.05-0.12$) with $T_c = 26$ K. *J. Am. Chem. Soc.* **2008**, *130*, 3296–3297.
3. Johrendt, D.; Pöttgen, R. Pnictide Oxides: A New Class of High-T_c Superconductors. *Angew. Chem., Int. Ed.* **2008**, *47*, 4782–4784 and references cited therein.
4. Chen, X. H.; Wu, T.; Wu, G.; Liu, R. H.; Chen, H.; Fang, D. F. Superconductivity at 43 K in $SmFeAsO_{1-x}F_x$. *Nature* **2008**, *453*, 761–762.
5. Rotter, M.; Tegel, M.; Schellenberg, I.; Hermes, W.; Pöttgen, R.; Johrendt, D. Spin-Density-Wave Anomaly at 140 K in the Ternary Iron Arsenide $BaFe_2As_2$. *Phys. Rev. B* **2008**, *78*, 020503–20507.
6. Alireza, P. L.; Ko, Y. T. C.; Gillett, J.; Petrone, C. M.; Cole, J. M.; Lonzarich, G. G.; Sebastian, S. E. Superconductivity Up to 29 K in $SrFe_2As_2$ and $BaFe_2As_2$ at High Pressures. *J. Phys.: Condens. Matters* **2009**, *21*, 012208–012212.
7. Chu, C. W.; Chen, F.; Gooch, M.; Guloy, A. M.; Lorenz, B.; Lv, B.; Sasmal, K.; Tang, Z. J.; Tapp, J. H.; Xue, Y. Y. The Synthesis and Characterization of LiFeAs and NaFeAs. *Phys. C* **2009**, *469*, 326–331.
8. Wang, X. C.; Liu, Q. Q.; Lv, Y. X.; Gao, W. B.; Yang, L. X.; Yu, R. C.; Li, F. Y.; Jin, C. Q. The Superconductivity at 18 K in LiFeAs System. *Solid State Commun.* **2008**, *148*, 538–540.
9. Hsu, F. C.; Luo, J. Y.; Yeh, K. Y.; Chen, T. K.; Huang, T. W.; Wu, P. M.; Lee, Y. C.; Huang, Y. L.; Chu, Y. Y.; Yan, D. C.; et al. Superconductivity in the PbO-Type Structure α-FeSe. *Proc. Natl. Acad. Sci. U.S.A.* **2008**, *105*, 14262–14264.
10. Paglione, J.; Greene, R. L. High-Temperature Superconductivity in Iron-Based Materials. *Nat. Phys.* **2010**, *6*, 645–658.
11. Hiramatsu, H.; Katase, T.; Kamiya, T.; Hosono, H. Thin Film Growth and Device Fabrication of Iron-Based Superconductors. *J. Phys. Soc. Jpn.* **2012**, *81*, 011011(25 pages).
12. Hosono, H. Layered Iron Pnictide Superconductors: Discovery and Current Status. *J. Phys. Soc. Jpn.* **2008**, *77*), 1–8.
13. Lumsden, M. D.; Christianson, A. D. Magnetism in Fe-Based Superconductors. *J. Phys.: Condens. Matters* **2010**, *22*, 203203(24 pages) and references cited therein.
14. Stewart, G. R. Superconductivity in Iron Compounds. *Rev. Mod. Phys.* **2011**, *83*, 1589–1649 and references cited therein.
15. McQueen, T. M.; Huang, Q.; Ksenofontov, V.; Felser, C.; Xu, Q.; Zandbergen, H.; Hor, Y. S.; Allred, J.; Williams, A. J.; Qu, D.; Checkelsky, J.; et al. Extreme Sensitivity of Superconductivity to Stoichiometry in $Fe_{1+\delta}Se$. *Phys. Rev. B* **2009**, *79*, 014522(7 pages).
16. Margadonna, S.; Takabayashi, Y.; McDonald, M. T.; Kasperkiewicz, K.; Mizuguchi, Y.; Takano, T.; Fitch, A. N.; Suard, E.; Prassides, K. Crystal Structure of the New $FeSe_{1-x}$ Superconductor. *Chem. Commun.* **2008**, 5607–5611.
17. Gresty, N. C.; Takabayashi, Y.; Ganin, A. X.; McDonald, M. T.; Claridge, J. B.; Giap, D.; Mizuguchi, Y.; Takano, Y.; Kagayama, T.; Ohishi, Y.; et al. Structural Phase Transitions and Superconductivity in $Fe_{1+\delta}Se_{0.57}Te_{0.43}$ at Ambient and Elevated Pressures. *J. Am. Chem. Soc.* **2009**, *131*, 16944–16952.
18. Medvedev, S.; McQueen, T. M.; Troyan, I. A.; Palasyuk, T.; Eremets, M. I.; Cava, R. J.; Naghavi, S.; Casper, F.; Ksenofontov, V.; Wortmann, G.; et al. Electronic and Magnetic Phase Diagram of β-$Fe_{1.01}Se$ with Superconductivity at 36.7 K Under Pressure. *Nat. Mater.* **2009**, *8*, 630–633.
19. Margadona, S.; Takabayashi, Y.; Ohishi, Y.; Mizuguchi, Y.; Takano, Y.; Kagayama, T.; Nakagawa, T.; Takata, M.; Prassides, K. Pressure Evolution of the Low-Temperature Crystal Structure and Bonding of the Superconductor FeSe ($T_c = 37$ K). *Phys Rev. B* **2009**, *80*, 064506–064515.
20. Bezryadin, A. Quantum Suppression of Superconductivity in Nanowires. *J. Phys.: Condens. Matters* **2008**, *20*, 043202–043221.
21. Bezryadin, A.; Lau, C. N.; Tinkham, M. Quantum Suppression of Superconductivity in Ultrathin Nanowires. *Nature* **2000**, *404*, 971–974.
22. Tian, M.; Wang, J.; Snyder, J.; Kurtz, J.; Liu, Y.; Schiffer, P.; Mallouk, T. E.; Chan, M. H. W. Synthesis and Characterization of Superconducting Single-Crystal Sn Nanowires. *Appl. Phys. Lett.* **2003**, *8*, 1620–1622.

23. Moshchalkov, V. V.; Fritzsche, J. *Nanostructured Superconductors*; World Scientific Publishing Co. Pte. Ltd.: Singapore, 2011; p 257.
24. Araújo, M. A. N.; García-García, A. M.; Sacramento, P. D. Enhancement of the Critical Temperature in Iron Pnictide Superconductors by Finite-Size Effects. *Phys. Rev. B* **2011**, *84*, 172502.
25. Dauler, E. A.; Robinson, B. S.; Kerman, A. J.; Yang, J. K. W.; Rosfjord, K. M.; Anant, V.; Voronov, B.; Gol'tsman, G.; Berggren, K. K. Multielement Superconducting Nanowire Single-Photon Detector. *IEEE Trans. Appl. Supercond.* **2007**, *17*, 279–284.
26. Imanishi, Y.; Sato, T.; Higashi, T.; Sun, W.; Okubo, S. A Network of Superconducting Gravimeters Detects Submicrogal Coseismic Gravity Changes. *Science* **2004**, *306*, 476–478.
27. Hadfield, R. H. Single-Photon Detectors for Optical Quantum Information Applications. *Nat. Photonics* **2009**, *3*, 696–705.
28. Marsili, F.; Najafi, F.; Dauler, E.; Bellei, F.; Hu, X.; Csete, M.; Molnar, R. J.; Berggren, K. K. Single-Photon Detectors Based on Ultranarrow Superconducting Nanowire. *Nano Lett.* **2011**, *11*, 2048–2053.
29. Wendin, G.; Shumeiko, V. S. Toward Tunable Superconducting Electronics. *Science* **2001**, *292*, 231–232.
30. Shein, I. R.; Enyashin, A. N.; Ivanovskii, A. L. Nanotubes of Layered Iron-Based Superconductors: Simulations of Atomic Structure and Electronic Properties. *Comput. Mater. Sci.* **2011**, *50*, 824–827.
31. Wang, J. G.; Tian, M. L.; Kumar, N.; Mallouk, T. E. Controllable Template Synthesis of Superconducting Zn Nanowires with Different Microstructures by Electrochemical Deposition. *Nano Lett.* **2005**, *5*, 1247–1253.
32. Xu, K.; Heath, J. R. Long Highly-Ordered High-Temperature Superconductor Nanowire Arrays. *Nano Lett.* **2008**, *8*, 3845–3849.
33. Nath, M.; Parkinson, B. A. A Simple Sol−Gel Synthesis of Superconducting MgB_2 Nanowires. *Adv. Mater.* **2006**, *18*, 1865–1868.
34. Wu, Y.; Messer, B.; Yang, P. Superconducting MgB_2 Nanowires. *Adv. Mater.* **2001**, *13*, 1487–1489.
35. Oyler, K. D.; Ke, X.; Sines, I. T.; Schiffer, P.; Schaak, R. E. Chemical Synthesis of Two-Dimensional Iron Chalcogenide Nanosheets: FeSe, FeTe, Fe(Se,Te), and $FeTe_2$. *Chem. Mater.* **2009**, *21*, 3655–3661.
36. Pol, S. V.; Pol, V. G.; Gedanken, A. Synthesis of Ferromagnetic Core-Shell Nanofibers. *J. Phys. Chem. C* **2007**, *111*, 16781–16786.
37. Han, Y.; Li, W. Y.; Cao, L. X.; Zhang, S.; Xu, B.; Zhao, B. R. Preparation and Superconductivity of Iron Selenide Thin Films. *J. Phys.: Condens. Matters* **2009**, *21*, 235702–235706.
38. Hamdadou, N.; Bernede, J. C.; Kheli, A. Preparation of Iron Selenide Films by Selenization Technique. *J. Cryst. Growth* **2002**, *241*, 313–319.
39. Williams, A. J.; McQueen, T. M.; Cava, R. J. The Stoichiometry of FeSe. *Solid State Commun.* **2009**, *149*, 1507–1509.
40. Zhou, S. M.; Lou, S. Y.; Wang, Y. Q.; Chen, X. L. Synthesis of Ordered α-FeSe Nanorod Array by CVD and Its High T_c. *Mater. Lett.* **2011**, *65*, 1741–1747.
41. Patterson, A. L. The Scherrer Formula for X-ray Particle Size Determination. *Phys. Rev.* **1939**, *56*, 978–981.
42. Jankovic, L.; Gournis, D.; Trikalitis, P. N.; Arfaoui, I.; Cren, T.; Rudolf, P.; Sage, M. -H.; Palstra, T. T. M.; Kooi, B.; Hosson, J. D.; et al. Carbon Nanotubes Encapsulating Superconducting Single-Crystalline Tin Nanowires. *Nano Lett.* **2006**, *6*, 1131–1135.
43. Kim, J. H.; Oh, N.; Kim, C. K.; Yoon, C. S. Area-Selective Growth of Amorphous Carbon Nanofibers *via* Catalytic Decomposition of Polyimide Thin Film. *Chem. Commun.* **2007**, 4018–4020.
44. Kwok, K.; Chiu, W. K. S. Growth of Carbon Nanotubes by Open-Air Laser-Induced Chemical Vapor Deposition. *Carbon* **2005**, *43*, 437–446.
45. Okamoto, H.; Massalski, T. B. The Au−Pd (Gold−Palladium) System. *Bull. Alloy Phase Diagram* **1985**, *6*, 229–235.
46. Okamoto, H.; Massalski, T. B.; Swartzendruber, L. J.; Beck, P. A. The Au−Fe (Gold−Iron) System. *Bull. Alloy Phase Diagram* **1984**, *5*, 592–600.
47. Raub, E.; Beeskow, H.; Loebich, O. The Iron−Palladium Phase Diagram below 950 °C. *Z. Metallkd.* **1963**, *54*, 549–552.
48. Takabataki, T.; Ishikawa, M.; Jorda, J. L. Superconductivity and Phase Relations in the Pd-Se System. *Tech. Rep. ISSP (Tokyo, Jpn)* **1987**, *134*, 79–89.